

See discussions, stats, and author profiles for this publication at: <https://www.researchgate.net/publication/369317136>

Spontaneous Formation of an Internal Shear Band in Ice Flowing over Topographically Variable Bedrocks

Preprint · March 2023

DOI: 10.22541/essoar.167898501.11505896/v1

CITATIONS

0

READS

103

6 authors, including:



Ludovic Räss

ETH Zurich

40 PUBLICATIONS 325 CITATIONS

[SEE PROFILE](#)



Frederic Herman

University of Lausanne

198 PUBLICATIONS 5,321 CITATIONS

[SEE PROFILE](#)



Jenny Suckale

Stanford University

101 PUBLICATIONS 1,289 CITATIONS

[SEE PROFILE](#)

Some of the authors of this publication are also working on these related projects:



Tectonics [View project](#)



Alpine excavations and the phase rule under heterogeneous pressure. [View project](#)

Spontaneous Formation of an Internal Shear Band in Ice Flowing over Topographically Variable Bedrocks 2

Emma Liu¹, Emma Weijia Liu², Ludovic Räss³, Frédéric Herman⁴, Yury Podladchikov⁵, and Jenny Suckale^{2,4}

¹Affiliation not available

²Geophysics Department, Stanford University

³Laboratory of Hydraulics, Hydrology and Glaciology (VAW), ETH Zurich

⁴Institute of Earth Surface Dynamics, University of Lausanne

⁵Institute of Earth Sciences, University of Lausanne

March 16, 2023

Spontaneous Formation of an Internal Shear Band in Ice Flowing over Topographically Variable Bedrocks

Emma Weijia Liu¹, Ludovic Räss^{2,3}, Frédéric Herman⁴, Yury Podladchikov⁵,
Jenny Suckale¹

¹Geophysics Department, Stanford University, USA

²Laboratory of Hydraulics, Hydrology and Glaciology (VAW), ETH Zurich, Switzerland

³Swiss Federal Institute for Forest, Snow and Landscape Research (WSL), Switzerland

⁴Institute of Earth Surface Dynamics, University of Lausanne, Switzerland

⁵Institute of Earth Sciences, University of Lausanne, Switzerland

Key Points:

- Ice flowing over a rough basal topography may spontaneously develop an internal shear band on topographical highs.
- The shear strain rate localization and shear heating in the internal shear band is amplified by a non-linear rheology.
- We identify two competing mechanisms that affect the energy balance near the bedrock: vertical advective cooling and internal shear heating.

Abstract

The dramatic acceleration of ice surface speed from upstream to downstream is a noticeable feature in many ice streams and glaciers. This speed-up is thought to be associated with a transition from internal, distributed deformation to highly localized deformation at the ice-bedrock interface, but the physical processes governing this transition remain unclear. Here, we argue that basal topography amplifies the feedback between shear heating and localization, leading to the spontaneous formation of an internal shear band for a non-linear rheology. We model the thermo-mechanical ice flow over a simplified basal topography using a high-resolution Stokes solver. To capture the interactions between ice and rock, we implement an Immersed Boundary Method and use a level-set approach to represent the free surface of the ice. Our results suggest that an internal shear band can form on topographical highs, continuously heating the basal ice and may gradually enable a transition to basal sliding. This effect depends sensitively on rheology, with the composite rheology by Goldsby and Kohlstedt (2001) amplifying shear heating notably.

Plain Language Summary

On its way towards the ocean, ice speeds up dramatically from less than one meter per year inland to up to a kilometer per year downstream. In this paper, we investigate the physical processes controlling this speed-up. More specifically, we focus on the role that the bedrock topography underneath the ice might play to facilitate this transition. We use a two-dimensional numerical model to simulate the temperature distribution and deformation within a slab of ice flowing down a ramp over a simplified topography. We find that including basal topography could lead to the development of internal shear band located on top of topographical highs. Around half of the total shear deformation within the ice occurs within this band. We compare our model results to borehole measurements from Greenland and find evidence that supports the existence of a shear band.

1 Introduction

The world's two ice sheets, Antarctica and Greenland, discharge most of their ice mass through fast-moving ice stream and mountain glaciers (Joughin, Smith, Howat, Scambos, & Moon, 2010; Rignot et al., 2011). As it approaches the ocean, ice moves at high speeds of up to a kilometer per year in some ice stream and glaciers (Rignot et al., 2002; Joughin et al., 2003; Mouginot et al., 2014), but near the ice divide, ice moves at low speeds of about 1 m/yr (Rignot et al., 2011). The speed-up is thought to be associated with a transition from flow through internal, distributed deformation to sliding, accommodated by highly localized deformation at the ice-bedrock interface (Clarke, 1987; Whillans et al., 1987). This transition from slow flow inland to rapid sliding in outlets is known as the flow-to-sliding transition or the onset of sliding.

One potential explanation for the flow-to-sliding transition is to invoke thawing of the bed through the creep instability, as first suggested by Robin (1955): Ice moving over a temperate bed can slide while ice frozen onto the bed must instead deform entirely internally. If the ice is initially frozen to bed, the internal deformation is most pronounced near the bed, where it could increase the internal temperature high enough to bring the ice-bedrock interface to its pressure melting point and enable sliding over a lubricated bed (Clarke et al., 1977; Yuen & Schubert, 1979). However, it remains unclear whether this thermo-mechanical feedback provides a viable explanation for the initiation and transition to sliding, as first mentioned in Nye (1971) and investigated further by Fowler and Larson (1980), Fowler (2001), Bueler and Brown (2009), and Mantelli et al. (2019).

Fowler and Larson (1980) showed that the solution of the steady state flows of glacier and ice sheets is unique if neglecting advection. This finding implies that the non-linear shear heating term alone, which couples the momentum and temperature equations, is unlikely to cause the instability. Fowler (2001) provided a more detailed argument of the thermal implications of a transition from flow-to-sliding with the neglect of advection, arguing that the local conservation of flux implies a reduction in shearing, translating into less energy release and refreezing. However, temperature in ice diffuses away slowly, raising doubts about the immediacy of this effect. Instead of diffusion, Bueler and Brown (2009) identified the advection of cold ice to the warm bed as the main impediment for a sudden transition to sliding; an argument further developed and simulated by Mantelli et al. (2019).

On the other hand, the work by Bueler and Brown (2009) and Mantelli et al. (2019) shows that for a sudden switch from flow-to-sliding using a depth-averaged viscosity or simply a linear viscosity, the cooling associated with thinning suppresses the creep instability. This insight highlights the importance of identifying not only the nature of the instability itself, but also the spatial scale over which it occurs. Bueler and Brown (2009) propose a cure by including an ad-hoc smoothing of the advection velocity, and Mantelli and Schoof (2019) invokes sub-temperate sliding to explain a spatially extended transition zone. The possibility of sub-temperate sliding is supported by recent laboratory experiments (McCarthy et al., 2017). While sub-temperate sliding is probably happening, there is an additional process not considered in idealized process-based models (Mantelli et al., 2019; Mantelli & Schoof, 2019) that could explain the missing spatial scale and is ubiquitous in the field: the topography of the subglacial bedrock.

The goal of this paper is to understand the impact of topographically uneven hard bedrock on ice flow acceleration by quantifying shear localization in the vicinity of the bedrock using numerical simulations. Our numerical model builds on recent advances in simulating the thermo-mechanical deformation of ice at high resolution implemented in FastICE v1.0 (Räss et al., 2020). We add to the original release of FastICE v1.0 by incorporating a free surface and variable basal topography since both are critical for the physical process that we aim to understand. We capture the free ice surface using a Level Set representation (Osher & Sethian, 1988; Sethian & Smereka, 2003) and the basal topography through an Immersed-Boundary Method (Peskin, 1972, 2002). We also generalize the rheology model in FastICE v1.0 from the classical Glen law (Glen, 1955) to a composite rheology identified in recent laboratory experiments (Goldsby & Kohlstedt, 2001).

Field observations motivate our focus on basal topography as a potentially important contributor to the flow-to-sliding transition: The initiation of streaming flow appears to coincide with changes in the basal topography at several locations, e.g., the Northeast Greenland Ice Stream (NEGIS) (Bamber et al., 2001), the Siple Coast Ice Streams (Siegert et al., 2004), and the Institute Ice Stream (Bingham & Siegert, 2007). Figure 1 shows NEGIS as an example. As ice moves towards the ocean, the basal topography becomes more pronounced (Figure 1 a) and the surface speed increases as the ice stream broadens (Figure 1 b). The location where ice speed starts increasing rapidly around 170 km downstream correlates roughly with the height of basal topography increasing (Figure 1 c) Overall however, the relationship between the vertical roughness of the bedrock, defined as the root mean square of the mean elevation of the bedrock (Li et al., 2010; Cooper et al., 2019), and surface speed is far from simple.

The spatial scale over which topographical highs varies prior to 170 km downstream is tens of meters, see Figure 1 (a). This scale is small as compared to the ice thickness of several hundred meters, but larger than the small-scale roughness of a few meters considered in existing sliding laws (e.g., Weertman, 1957; Nye, 1959; Lliboutry, 1968; Fowler, 2010; Schoof, 2005; Bindshadler, 2006; Petrat et al., 2012). Complementing this representation of small-scale roughness, existing ice-dynamics models such as Elmer (e.g.

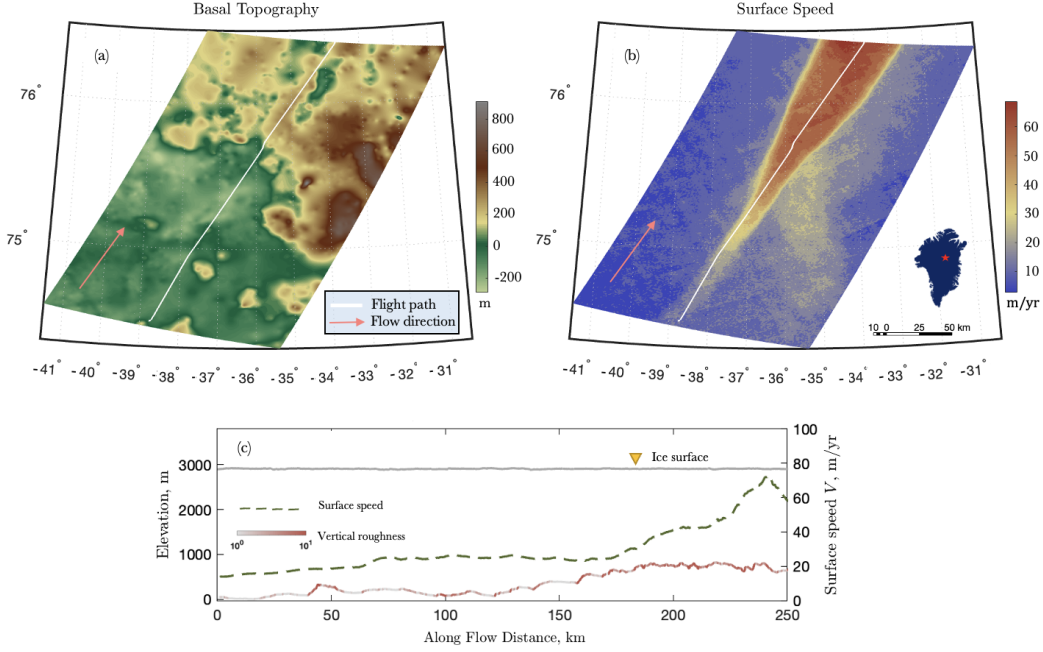


Figure 1. Basal topography and surface speed at NEGIS. (a): Basal topography contour from BedMachine 3 (Morlighem et al., 2017). (b) Surface speed contour from MEaSUREs NSIDC (Joughin, Smith, Howat, & Scambos, 2010). (c) Surface speed (dashed line) change with the basal topography (red-to-white solid line) along flight path, indicated as the white lines in (a) and (b). The red-to-white color change indicates the vertical roughness as described more in Section 4. The ice surface is shown as a grey solid line. We obtained the basal topography and ice thickness in (c) from Franke et al. (2021).

Gagliardini et al., 2013), SICOPOLIS (e.g. Greve, 1997a, 1997b), and PISM (e.g. Winkelmann et al., 2011; Martin et al., 2011) are well suited to capture large-scale topographic variations by using meshes fitted to large-scale topography. The contribution of our work is to advance our understanding and ability to model the ice-dynamics implications of intermediate-scale topographic variations of hundreds of meters in wavelength and tens of meters in amplitude.

Figure 1 exemplifies an interesting correlation between basal topography and surface speed, but it would be challenging to test a process-based model results against this data alone, because this regional-scale data does not constrain the physical processes occurring within the ice. Borehole measurements of ice properties with depth provide a compelling complement, for example the data obtained at the West Margin of Greenland (Maier et al., 2019; Doyle et al., 2018). These measurements show a high shear strain rate concentrated within around 10–50 m above the bedrock, but nearly zero shear strain rate is observed at bedrock. Such a high localization of shear strain rate in the interior of the ice evinces the possibility of internal sliding interface. We compare against this data to evaluate how the presence of an internal shear band could be reflected in observations.

2 Methods

To approximate the thermo-mechanical deformation within a slab of ice flowing over a rough hard bedrock in the downstream direction x (Figure 2 a), we neglect variabil-

ity in the transverse direction y . This choice reduces our modeling domain to a two-dimensional, along-flow cut through the three-dimensional ice slab along the thick black line (Figure 2 a). The depth direction z is oriented vertically upwards from the bedrock. The origin of the axes ($x = 0, z = 0$) locates at the bedrock of the flow inlet. The size of the model domain is $[0, L] \times [0, H]$, and it is tilted at an angle α . To represent basal topography, we adopt a highly idealized sinusoidal contour $z = A \sin(\lambda/2\pi x)$ with an amplitude A and a wavelength λ similar to the setup in the seminal paper by Nye (1969). We include a low-viscosity phase on top of the ice to mimic the presence of air, which allows ice thickness to change spatially and temporally.

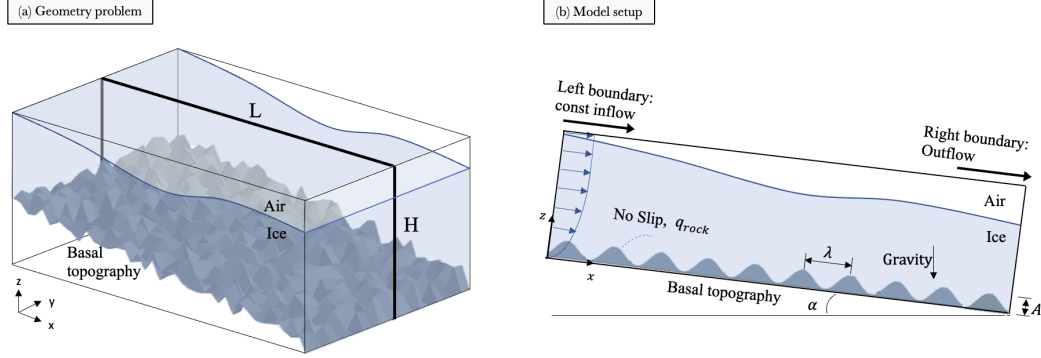


Figure 2. Model geometry of ice sheet flowing over rough hard bedrock. (a) The general case of a slab of ice flowing over rough hard bedrock in three-dimensions with a free surface. (b) The two-dimensional model setup with a sinusoidal basal topography and a free surface.

We capture the depth-dependent thermo-mechanical ice deformation implementing an incompressible viscous Stokes solver using the time-dependent implicit pseudo-transient methods (Räss et al., 2022) and the finite difference discretization developed by Räss et al. (2020). To prescribe the basal ice-bedrock boundary condition, we implement the Immersed Boundary Method, a fictitious domain method that allows to treat fluid and structural domains separately (Peskin, 1972, 2002). To incorporate the free surface boundary condition, we use the Level Set Methods, an implicit description for moving fronts further advected with the local fluid velocity (Sethian & Smereka, 2003; Osher et al., 2004).

2.1 Thermo-mechanical Model

We describe ice as an incompressible, non-linear, viscous fluid with a temperature-dependent rheology. The momentum equations are

$$\frac{\partial \tau_{ij}}{\partial x_j} - \frac{\partial p}{\partial x_i} + F_i = 0, \quad \tau_{ij} = 2\eta \dot{\epsilon}_{ij}, \quad (1)$$

where $F_i = \rho g(\sin \alpha, \cos \alpha)$ is the gravitational body force at a tilted angle α , p is isotropic pressure, τ_{ij} is the deviatoric stress tensor, $\dot{\epsilon}_{ij}$ is the shear strain rate tensor, and η is the ice viscosity. Reducing the model to two dimensions implies that all components in the transverse direction y are zero. The only nonzero shear strain rate and shear stress are $\dot{\epsilon}_{zx}$ and τ_{zx} , respectively.

Ice flows into the domain from the left boundary over an undeforming hard bedrock, and exits at the right boundary. The momentum balance along the flow at steady state is

$$\eta(z) \frac{\partial u}{\partial z} = \rho g (H - z) \sin \alpha. \quad (2)$$

To obtain an analytical expression for the inflow velocity profile, we assume a linear viscosity profile between the viscosity at the bed, η_b , and the viscosity at the surface, η_s . Integrate equation (2), we have the analytical inflow velocity

$$u_{\text{inlet}} = \frac{\rho g \sin \alpha}{K^2} [\eta_b \log(\eta_b + Kz) + KH \log(\eta_b + Kz) - Kz] + C, \quad (3)$$

where $K = (\eta_s - \eta_b)/H$, and C is the integration constant such that the velocity at bed is zero. When viscosity is constant throughout the domain, $\eta_s = \eta_b = \eta_0$, the analytical inflow velocity simplifies to a parabolic velocity profile $u_{\text{inlet}} = \rho \sin \alpha / \eta_0 (Hz - 0.5z^2)$.

At the outlet, we adapt the outflow boundary condition from Orlanski (1976)

$$\frac{\partial u}{\partial t} + U \frac{\partial u}{\partial x} = 0, \quad (4)$$

where U is the propagation velocity. Following the approach by Kreiss (1968), we estimate it numerically by calculating the propagation velocity between neighboring grid points $U = \Delta x / \Delta t$, where Δx and Δt are the spatial and temporal grid sizes, respectively. The extrapolated velocity at the outlet boundary is then

$$u_{\text{Nx}}^{n_t} = 2u_{n_x-1}^{n_t-1} - u_{n_x-2}^{n_t-2}, \quad (5)$$

where n_x is the boundary point and n_t is the current time step.

At the ice surface, we assume that the atmospheric pressure is negligible relative to the pressure in the ice column, implying a stress-free surface

$$\sigma_{ij} n_j = 0. \quad (6)$$

where n_j is the normal vector to the ice surface, σ_{ij} is the Cauchy stress tensor, obtained by combining the isotropic pressure p and the deviatoric stress τ_{ij} .

At the ice-bedrock interface, we assume ice is frozen to bed along the ice-bedrock interface and impose a no-slip boundary condition. We implement this boundary condition using the Immersed Boundary Methods. The details are discussed in Section 2.3.

Our thermal model takes into account the effects of diffusion, advection, shear heating, and melt water weakening. We curtail the temperature at $T_m = -0.1^\circ\text{C}$ and estimate the melt rate with the latent heat. The energy equation is given by

$$\rho c_p \left(\frac{\partial T}{\partial t} + u_i \frac{\partial T}{\partial x_i} \right) = \frac{\partial}{\partial x_i} \left(\kappa \frac{\partial T}{\partial x_i} \right) + 2\tau_E \dot{\epsilon}_E - L\dot{m}, \quad (7)$$

where c_p is the specific heat of ice, κ is the thermal conductivity, τ_E and $\dot{\epsilon}_E$ are effective shear stress and effective shear strain rate, respectively. The term $2\tau_E \dot{\epsilon}_E$ represents

shear heating, $L\dot{m}$ captures the energy required for melting where $L = 0.366 \times 10^6 \text{ J/kg}$ is the latent heat, and \dot{m} is the generated melt water flux.

In the temperate zone where temperature is around the melting point, we assume that the shear heating $2\tau_E \dot{\epsilon}_E$ is absorbed for the phase change from ice to water (Suckale et al., 2014; Räss et al., 2020). The temperature in the temperate zone can hence not exceed the pressure melting point, leading to the simplified energy equation

$$\rho c_p \left(\frac{\partial T}{\partial t} + u_i \frac{\partial T}{\partial x_i} \right) = \frac{\partial}{\partial x_i} \left(\kappa \frac{\partial T}{\partial x_i} \right) + 2\tau_E \dot{\epsilon}_E f(T - T_m), \quad (8)$$

where f is the logistic function in the form of

$$f(T - T_m) = 1 - \tanh(-0.5(T - T_m)). \quad (9)$$

The logistic function serves as an indicator of how close the ice temperature is to the melting point T_m . When the temperature has reached the melting point, i.e., $f(T - T_m) = 0$, all shear heating is absorbed to for the phase change from ice to water, and no net heat source is added to energy equation.

At the surface, we impose a constant atmospheric temperature at $T_{\text{surf}} = -26^\circ\text{C}$. At the ice-bedrock interface, we impose a constant geothermal heat flux, which is discussed in Section 2.3.

The time dependence of the problem comes from the free surface evolution and from the energy equation because the shear heating, diffusion and advection terms are transient. At each physical time step, following the approach by Räss et al. (2020), we use the pseudo-transient method to solve the system of coupled momentum equations (1) and energy equation (8) iteratively until the continuity residual, $\partial p / \partial \tau_p$, momentum residual, $\partial u_i / \partial \tau_u$, and temperature residual, $\partial T / \partial \tau_T$, are minimized. Thus, the governing equations in a residual form are

$$\frac{\partial p}{\partial \tau_p} = -\frac{\partial u_i}{\partial x_i}, \quad (10)$$

$$\frac{\partial u_i}{\partial \tau_u} = \frac{\partial \tau_{ij}}{\partial x_j} - \frac{\partial p}{\partial x_i} + F_i, \quad (11)$$

$$\frac{\partial T}{\partial \tau_T} = -\frac{\partial T}{\partial t} - u_i \frac{\partial T}{\partial x_i} + \frac{1}{\rho c_p} \left(\frac{\partial}{\partial x_i} \left(\kappa \frac{\partial T}{\partial x_i} \right) + 2\tau_E \dot{\epsilon}_E f(T - T_m) \right), \quad (12)$$

where τ presents the pseudo time step, and t represents physical time step.

The key limiting factor of the convergence rates of equation (10) to (12) is the convergence rate of the ice viscosity. During the pseudo iterations, we do not evolve the ice surface. After the residuals fall below the defined thresholds indicating that the numerical solution has reached steady state, we advect the free surface with the local ice velocity. The details of the advection of the free surface is presented in Section 2.3.

2.2 Rheology Model

The rheology governs the thermo-mechanical deformation of ice and hence the strain localization that might occur within the ice column. In our model, we compare three different constitutive relations, namely: a Newtonian rheology, a power law rheology, and the composite rheology by Goldsby and Kohlstedt (2001). In the Newtonian case, viscosity remains constant spatially and temporally, decoupling the momentum and energy equations. For the power law rheology, we use Glen's law

$$\dot{\epsilon}_{ij} = A T_{II}^{n-1} \exp \left(-\frac{Q}{R(T_{\text{surf}} + T)} \right) \tau_{ij} , \quad (13)$$

where the stress exponent n is 3 (Glen, 1952, 1955), A is pre-exponential factor, Q the activation energy, R the universal gas constant, and T_{surf} the surface temperature.

For the composite rheology, we follow Goldsby and Kohlstedt (2001) and describe the ice rheology as a combination of four deformation mechanisms: diffusion creep, basal slip, grain boundary sliding (GBS), and dislocation creep:

$$\dot{\epsilon} = \dot{\epsilon}_{\text{diff}} + (1/\dot{\epsilon}_{\text{basal}} + 1/\dot{\epsilon}_{\text{GBS}})^{-1} + \dot{\epsilon}_{\text{disl}} . \quad (14)$$

The diffusional flow

$$\dot{\epsilon}_{\text{diff}} = \frac{42V_m D_\nu}{RT} \tau_E \exp \left(\frac{-Q_{\text{diff}}}{RT_h} \right) \quad (15)$$

dominates at lower stresses with $n = 1$. Upon increasing stresses, basal slip becomes the controlling mechanism with $n = 2.4$

$$\dot{\epsilon}_{\text{basal}} = A_{\text{basal}} \tau_E^n \exp \left(-\frac{Q_{\text{basal}}}{RT_h} \right). \quad (16)$$

At higher stresses, basal slip is accommodated by GBS with $n = 1.8$ (but fairly low activation energy) until dislocation creep with $n = 4$, becomes the primary deformation mechanism at the very high stresses. We capture the latter two mechanisms with the same power law relationship

$$\dot{\epsilon}_{\text{GBS}} = A_{\text{GBS}} \tau_E^n \exp \left(-\frac{1}{R} \left(\frac{Q_{\text{GBS}} - Q_1}{T_{h,\text{GBS}}^*} - \frac{Q_{\text{GBS}}}{T_h} \right) \right), \quad (17)$$

$$\dot{\epsilon}_{\text{disl}} = A_{\text{disl}} \tau_E^n \exp \left(-\frac{1}{R} \left(\frac{Q_{\text{disl}} - Q_1}{T_{h,\text{disl}}^*} - \frac{Q_{\text{disl}}}{T_h} \right) \right). \quad (18)$$

In the above equations, temperature with a h subscript denotes temperature adjusted for pressure-melting $T_h = T + p_0 p$, where p_0 is the pressure heating coefficient. Temperature with a $*$ superscript denotes the activation threshold temperature. The parameters used in the composite rheology (Goldsby & Kohlstedt, 2001) are summarized in Table 1.

One challenge in implementing the composite rheology is that the pre-exponential factor, A , is difficult to constrain experimentally or observationally, partly because it captures several different physical processes. The parameter combines an integrated effects of grain size, temperature, fabrics, and other variables (Paterson, 1994). In our model, A depends only on temperature and interstitial water content, and we neglect other dependencies like grain size, mostly because limited data exists to constrain these.

To capture the viscosity-weakening effect of interstitial water, we define an additional parameter A_w . According to Duval et al. (1977), an increase in water content from 0% to 1% can lead to a drop in effective ice viscosity by a factor of approximately 5. In our model, we use the same logistic function from equation (9) that reads $A_w = (1 - f(T - T_m))$ in the energy equation to capture viscous weakening in the presence of water for both Glen's law and the composite rheology by Goldsby and Kohlstedt (2001).

Thus, our implementation of the pre-factor is then $A = A_0 A_w$, where A_0 comes from the temperature dependency. For example, in the basal slip regime, $A_{\text{basal}} = A_{0,\text{basal}} A_{w,\text{basal}}$.

Table 1. The parameters used in the composite rheology (Goldsby & Kohlstedt, 2001)

Symbol	Parameter	Value	Unit
$A_{0,\text{basal}}$	basal slip pre-exponential factor	7.087×10^{-7}	N/A
$A_{0,\text{disl}}$	dislocation pre-exponential factor	3.12×10^{-19}	N/A
$A_{0,\text{GBS}}$	GBS pre-exponential factor	5.42×10^{-13}	N/A
D_ν	volume diffusional coefficient	9.1×10^{-4}	m ² /s
n	rheology exponent	1 (diffusional), 1.8(GBS) 2.4(basal slip), 4(dislocation)	N/A
p_0	pressure heating coefficient	7×10^{-8}	K/Pa
Q_{basal}	basal slip activation energy	6×10^4	J/mol
Q_{diff}	diffusional activation energy	5.94×10^4	J/mol
Q_{disl}	dislocation slip activation energy	6.4×10^4 if $T_h < T_H^*$ 2.2×10^5 if $T_h \geq T_H^*$	J/mol
Q_{GBS}	GBS activation energy	4.9×10^4 if $T_h < T_H^*$ 1.97×10^5 if $T_h \geq T_H^*$	J/mol
R	universal gas constant	8.314	J/(mol · K)
$T_{h,\text{GBS}}^*$	threshold activation temperature for GBS	257	K
$T_{h,\text{disl}}^*$	threshold activation temperature for dislocation	255	K
V_M	molar volume	1.97×10^{-5}	m ³ /kmol

2.3 Implementation of the Basal Interface and Free Surface

To capture the mechanical and thermal interactions along the ice-bedrock irregular interface Γ , we integrate the Immersed Boundary Method (IBM) developed by Peskin (Peskin, 1972, 2002) into the Stokes solver. The IBM is a fictitious domain method that discretizes the ice and rock phases with Eulerian and Lagrangian approaches, respectively. The discretization process for each phase is independent of each other and does not require body-fitted meshes. As illustrated in Figure 3 (a), two sets of discretizations are used: The Lagrangian points are attached to and stay on the outline of bed shape Γ . In contrast, the Eulerian mesh spans the whole domain, Ω_i , including the area occupied by the solid structure.

The general idea of IBM is to solve the ice governing equation (1) and (8) on a Eulerian grid imposed on the ice domain, Ω_i , with a correction on the ice-bedrock interface Γ at each intermediate time step to impose the boundary condition. Here, we use the direct forcing implementation of IBM developed by Uhlmann (2005). The implementation is decomposed into four steps. First, advance the governing equation (10) to (12) and equation (8) for one pseudo time step forward without considering the submerged bed rock. We refer to this solution as the intermediate fields $u^{n+1/2}$ and $T^{n+1/2}$

$$\frac{u_i^{n+1/2} - u_i^n}{\Delta \tau_u} = \left(\frac{\partial \tau_{ij}}{\partial x_j} \right)^n - \left(\frac{\partial p}{\partial x_i} \right)^n + F_i, \quad (19)$$

$$\frac{T_i^{n+1/2} - T_i^n}{\Delta \tau_T} = -\frac{\partial T}{\partial t} - \left(u_i \frac{\partial T}{\partial x_i} \right)^n + \frac{1}{\rho c_p} \left(\frac{\partial}{\partial x_i} \left(\kappa \frac{\partial T}{\partial x_i} \right) + 2\tau_E \dot{\epsilon}_E f(T - T_m) \right)^n \quad (20)$$

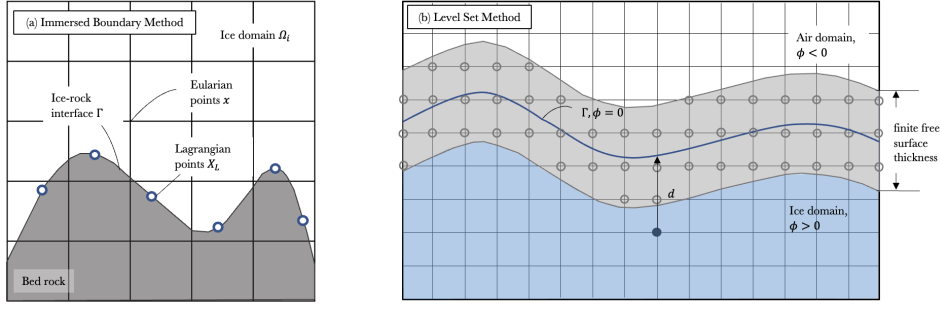


Figure 3. Illustration of Immersed Boundary Method and Level Set Method. (a): Treatment of the ice-bedrock interface. The spatial discretization of the ice domain, Ω_i , and bed shape, Γ . Ω_i is discretized in a Cartesian grid x . The ice-bedrock interface, Γ , is discretized using Lagrangian points X_L . (b): Treatment of the ice-air interface. The domain is divided into ice (blue) and air (white) domains using a level-set function with a finite but very small free surface thickness (light grey).

where the superscript n represents the current pseudo time step and $\Delta\tau$ represents the pseudo time step size.

Second, we use a regularized delta δ function (Peskin, 2002) to translate the intermediate quantities $u^{n+1/2}, T^{n+1/2}$ on the Eulerian points x to that on the Lagrangian points X_L . Dropping the superscript for simplicity, we have

$$U(X_L) = \sum u(x)\delta(x - X_L)dx dz, \quad Q(X_L) = \sum q(x)\delta(x - X_L)dx dz, \quad (21)$$

where $q = \partial T / \partial x_i$ denotes the heat flux, dx and dz are the horizontal and vertical grid size, and the lower case and upper letters represent Eulerian and Lagrangian quantities, respectively. The delta function is a continuous differentiable function that takes 1 if the Eulerian grid point is on the Lagrangian points point and 0 if far away, thus allowing a smooth transfer between the grids.

Third, we compute the volume forces F_U and F_Q required to achieve the desired boundary condition, in this case, the no-slip condition $U^d = 0$ and constant geothermal heating condition Q^d :

$$\frac{U^{n+1/2} - U^d}{\Delta t} = F_U^{n+1/2}, \quad \frac{Q^{n+1/2} - Q^d}{\Delta t} = F_Q^{n+1/2}. \quad (22)$$

Finally, we use the computed volume force to correct the intermediate fields u and T and obtain the velocity and temperature fields at the next pseudo time step

$$u^{n+1} = u^{n+1/2} + \frac{F_U^{n+1/2}}{\Delta V_{lag}}, \quad q^{n+1} = q^{n+1/2} + \frac{F_Q^{n+1/2}}{\Delta V_{lag}}, \quad (23)$$

where ΔV_{lag} is control volume of one Lagrangian points point. In our model, we select the number of Lagrangian points such that $\Delta V_{lag} \sim dx dz$.

The other interface that requires careful numerical treatment is the upper surface of the ice. Ice thins as it speeds up and the free surface moves downwards towards the

bed. While the movement itself is relatively slow and gradual, its thermal implications could be very important (e.g., Mantelli et al., 2019). To capture ice thinning, we represent the free surface as the level set of a higher dimensional distance function, as illustrated in Figure 3 (b), allowing us to handle the moving front implicitly as discussed in the books by Sethian (1999) and Osher et al. (2004). More specifically, the ice-air interface is defined as the zero-contour of a signed distance function ϕ

$$\phi(x) = \begin{cases} -d & \text{if } x \in \text{air}, \\ +d & \text{if } x \in \text{ice}. \\ 0 & \text{if } x \in \Gamma, \end{cases} \quad (24)$$

where d is the distance from the grid point to the interface. Across $\phi(x) = 0$, the density ρ , viscosity η , and thermal conductivity κ change

$$\rho(\phi) = \rho_a + (\rho_i - \rho_a)H(\phi), \quad (25)$$

$$\eta(\phi) = \eta_a + (\eta_i - \eta_a)H(\phi), \quad (26)$$

$$\kappa(\phi) = \kappa_a + (\kappa_i - \kappa_a)H(\phi), \quad (27)$$

where the subscript i denotes the material properties in the ice domain, subscript a denotes those in the air domain, and H is the Heaviside function defined as

$$H(\phi) = \begin{cases} 0 & \phi < -\epsilon, \\ \frac{1}{2} + \frac{\phi}{2\epsilon} + \frac{1}{2\pi} \sin \frac{\pi\phi}{\epsilon} & -\epsilon \leq \phi \leq \epsilon, \\ 1 & \phi > \epsilon, \end{cases} \quad (28)$$

with a smoothing length of $\epsilon = 3\Delta x$.

To evolve the location of the interface, we advect the level field using the general advection equation, also known as the level set equation:

$$\frac{\partial \phi}{\partial t} + u_n |\nabla \phi| = 0, \quad (29)$$

where u_n is the physical velocity in the normal direction. This equation moves the implicit front with the ice velocity field determined by the mechanical equations (1) at each physical time step. The spatial discretizations use first-order upwind, and the temporal discretizations use the second-order accurate Total Variation Diminishing Runge–Kutta schemes. Since the ice-air interface remains smooth at all times and thins only slightly as compared to the overall thickness of the ice sheet, sophisticated advection schemes such as extension velocities (Adalsteinsson & Sethian, 1999), topology-preservation techniques (Qin et al., 2015) or reinitialization (Osher et al., 2004) are not necessary in our case.

2.4 Verification

To verify the accuracy of our numerical method, we compare our numerical results to two analytical solutions, the circular inclusion test by Schmid and Podladchikov (2003) and the classic Nye solution for the velocity field in ice flowing over a wavy surface (Nye, 1969). These two benchmarks are complementary, because the circular-inclusion test is better suited for identifying spurious oscillations in the pressure field while the Nye solution represents a flow configuration more closely related to the dynamic problem we aim to understand here.

Following Schmid and Podladchikov (2003), we consider a circular solid inclusion immersed in a square domain with homogeneous fluid. We apply a pure shear boundary condition to the fluid domain and a no-slip to inclusion-fluid boundary. To evaluate the accuracy of the numerical scheme, we compare our numerical results to the two-dimensional analytical solutions of the pressure and velocity fields

$$v_x + iv_y = \epsilon R^2 \left(-\frac{1}{z} - \frac{z^3}{r^4} + R^2 \frac{z^3}{r^6} \right) + \dot{\epsilon} \frac{r^2}{z}, \quad (30)$$

$$P = 4\eta\epsilon \cos(2\theta) \frac{R^2}{r^2}, \quad (31)$$

where $z = x + iy = re^{i\theta}$, ϵ is the shear strain rate, η is the fluid viscosity and R is the radius of the inclusion. The boundary conditions applied are the pure shear strain rate

$$v_x = \dot{\epsilon}x, v_y = -\dot{\epsilon}y. \quad (32)$$

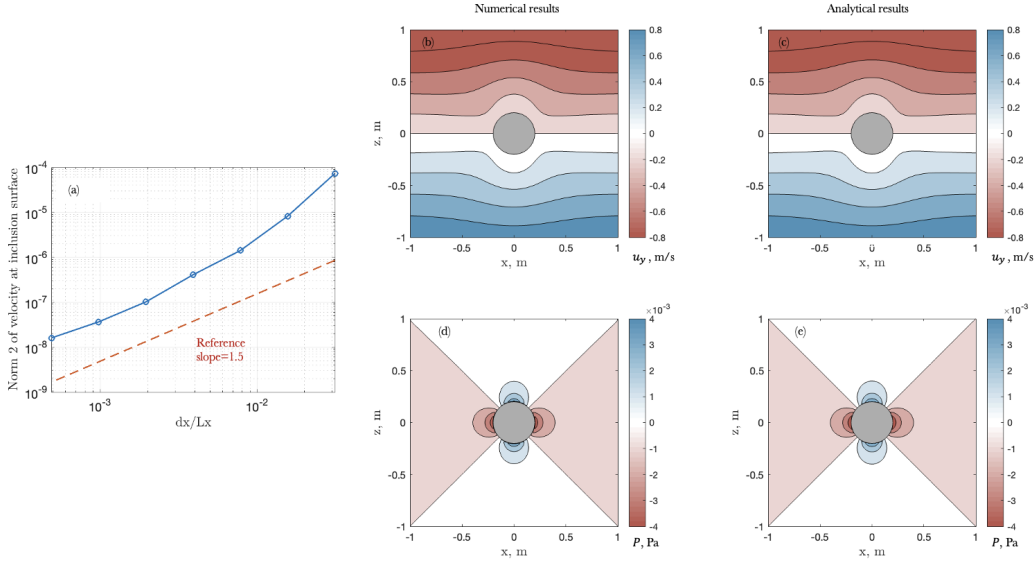


Figure 4. Spatial convergence test for the inclusion case. (a) The L2 norm of the velocity at the cylinder. (b) and (c): Vertical velocity in the analytical case and numerical case, respectively. The black solid lines in (b) and (c) represent the streamlines. (d) and (e): Pressure in the analytical case and numerical case, respectively. The resolution shown here is 512×512 .

We further test our model with Nye's analysis of the flow over wavy bed with a Newtonian fluid. We followed Nye (1969)'s model setting, and considered the bed shape in the form of a sine wave $z_0 = \epsilon a \sin(kx)$. The boundary condition is simple shear on the surface $[\tau_x, \tau_z] = [1, 0]$, periodic in the flow direction. Here, we limit our reference analytical solution to only first order $\mathcal{O}(\epsilon)$. The full solution can be found in Nye (1969). The analytical velocity fields to the first order are

$$u = U \left(1 + \epsilon a \beta k^2 \exp(-kz) \sin(kx) \right) + \mathcal{O}(\epsilon^2), \quad (33)$$

$$v = U \epsilon a \beta k (1 + kz) \exp(-kz) \cos(kx) + \mathcal{O}(\epsilon^2), \quad (34)$$

$$p = 2\eta U a \beta k^2 \exp(-kz) \cos(kx) + \mathcal{O}(\epsilon^2), \quad (35)$$

where U is the far field horizontal velocity, $\beta = k_*^2/(k_*^2 + k^2)$, and k_* stands for the characteristic wavenumber of regelation.

Figure 4 depicts the spatial convergences for the inclusion cases, where (b) and (c) compare the results of numerical and analytical vertical velocity fields, (d) and (e) compare the results of pressure fields, and (a) shows that the combination of the Stokes solver and IBM leads to the spatial accuracy around order 1.5. Figure 5 (a-b) shows the comparison between the numerical and analytical vertical velocity fields of the Nye’s case. In (c), we show the pressure comparison along the $z = 2.2$ m horizontal line.

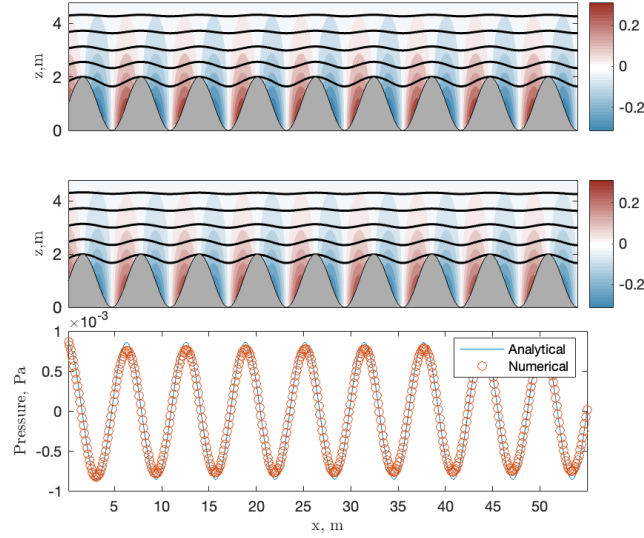


Figure 5. Comparison of numerical solutions against analytical solutions of Nye’s problem (Nye, 1969). (a): Vertical velocity in the analytical case. (b): Vertical velocity in the numerical case. The black solid lines in (a) and (b) represent the streamlines. (c): Pressure along the $z = 2.2$ m for both numerical and analytical cases. The resolution shown here is 512×128 .

3 Results

All simulation results presented in this paper include a free ice surface. One example of the ice surface evolving over time is shown in Figure 6. At the scale of the model domain, the ice-surface change is not immediately apparent, but a close-up view of the upper tens of meters of the domain clarifies that the surface is evolving if only by a few meters or less than 1% of the ice thickness. Given this small change and our focus on shear localization near the bed, we only plot the bottom part of our model domain in the remaining figures of this section.

3.1 Ice Flowing over Topography May Form an Internal Shear Band

To identify how basal topography affects internal deformation, we compare the thermo-mechanical deformation of ice flowing over an idealized sinusoidal topography to ice flow without topographical control (Figure 7). All other parameters and boundary conditions are set identically for the two cases. Here we use the composite rheology (Goldsby & Kohlstedt, 2001) and include water weakening in the effective viscosity as discussed in Section 2.1.

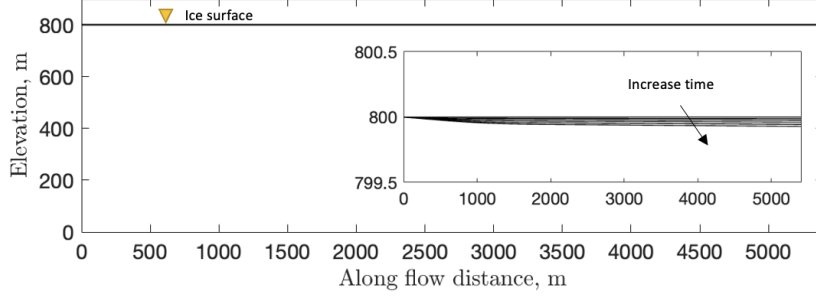


Figure 6. Ice surface evolution over 80 years on a flat bed. The subfigure shows a zoom in view of the ice surface evolution. The rheology used in this example is the Glen’s law.

Figure 7 (a) shows the case of ice (light grey) flowing over a sinusoidal topography (dark grey) for the lower portion of our model domain. The ice speeds up from left to right as indicated by the green velocity profiles at four different along-flow locations, where we compare the local velocity in dark green with inflow velocity in light green. This speed-up is facilitated by shear localizing increasingly on top of the topography as indicated in orange. The highest shear values occur on the topographical highs, effectively linking these up into a continuous zone of elevated shear strain rate. The control simulation of ice flowing over a flat topography is shown in Figure 7 (b). Similarly to Figure 7 (a), ice speeds up as it flows downstream, aided by shear strain rate in the immediate vicinity of the flat topography.

The main difference between the two simulations is how shear strain rate is distributed with depth (Figure 7 c). For the flat bed (Figure 7 b), the shear strain rate is highest nearest to the bed, whereas topography shifts the shear-rate maximum into the ice column to a depth that corresponds roughly to the height of the topographic peaks (Figure 7 a). Both modes of deformation are capable of generating approximately comparable surface speeds of around 100 m/yr, with the ice flowing over rough topography moving slightly faster at equal driving stress and basal resistance. Since the speed-up of the ice is gradual and not instantaneous, the cooling effect associated with ice thinning is not sufficient to prevent viscosity weakening in either of the simulations.

To quantify the share of total deformation accommodated within the ice as ice flows over the basal topography, we define R_d^* as the percentage of the internal deformation in the ice column to be the ratio of the integral of the shear strain rate from the bed up to some elevation z and the integral of the total shear strain rate in the entire ice column

$$R_d^* = \frac{\int_b^z \frac{\partial u}{\partial z}}{\int_b^s \frac{\partial u}{\partial z}} = \frac{u_z}{u_s}, \quad (36)$$

where subscripts d , b and s represent deformation, bed and surface, respectively. The superscript $*$ denotes a non-dimensional parameter. We use the term “shear band” to be a basal zone that accommodates the majority ($\geq 50\%$) of the total deformation in the ice column. We set the lower and upper bound of the internal shear band R_{dl}^* and R_{du}^* to 20% and 70%, respectively. Finally, we define the bandwidth B_w as the vertical distance between these two bounds in the ice column

$$B_w = z(R_{du}^*) - z(R_{dl}^*). \quad (37)$$

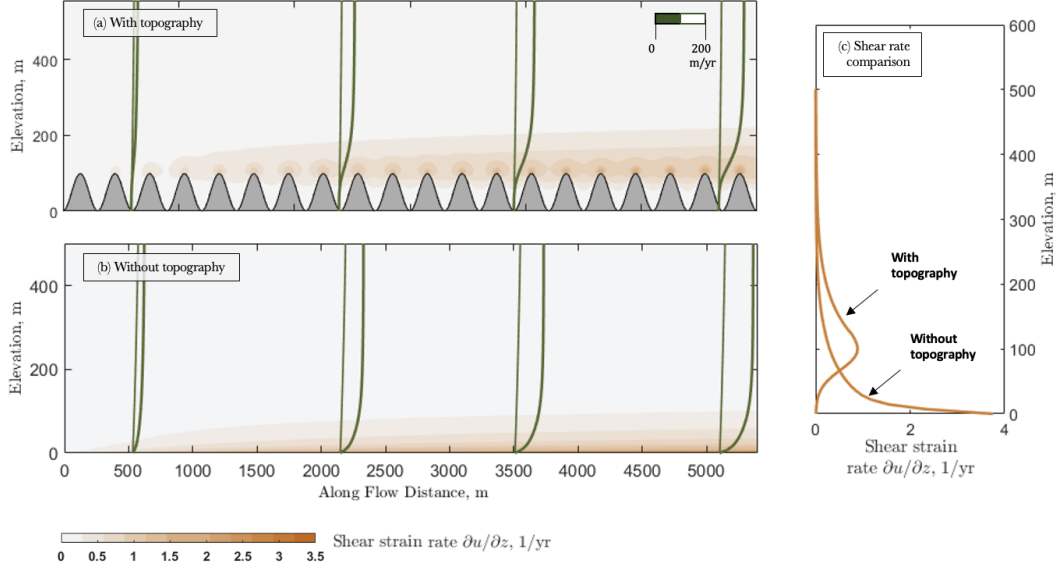


Figure 7. Role of basal topography in shear localization. (a) and (b): shear strain rate $\partial u / \partial z$ shown in the background contour for the case of with basal topography and without basal topography. The velocity profiles at different locations along the flow are shown in the dark green lines, with a reference inflow velocity in light green lines. (c): The shear strain rate profile at $x = 5000$ m for both cases.

Figure 8 shows how the shear band evolves within the model domain. Towards the left boundary, deformation is distributed relatively evenly as indicated by the 20% and 70% contour differing by several hundred meters in depth (Figure 8 a). As ice flows downstream, the lower limit of the shear band, $R_{dl}^* = 20\%$, stays on top of the basal topography shape and does not change depth much. This result highlights that the depth-distribution of deformation below the topographical highs remains relatively unaffected by the shear localization and ice speeds up mainly at and above the topographical highs. The upper limit $R_{du}^* = 70\%$ descends sharply, and then stabilizes around $z = 200$ m. For the case shown, the shear band has a width that is close to the amplitude of the sinusoidal bed shape, and accommodates approximately half of the total shear strain rate.

In the control case without topography, we find a similar transition from distributed to localized deformation, but the shear band is located at the bed instead of within the ice column. The shear strain rate is maximal at the ice-bedrock interface with the $R_{dl}^* = 20\%$ contour remaining very close to and almost at the bed (Figure 8 b). One remarkable difference is that without topography, all depths of the ice, from the surface to the ice-bedrock interface, is affected by the shear localization and the surface speed-up. Figure 8 (c) shows the ratio of the shear band bandwidth B_w to the ice thickness H . Initially, the shear-band width constitutes about 50%-60% of the ice thickness for both cases. It decreases rapidly in the downstream direction, and finally stabilizes at a width of approximately 10% of the ice thickness.

3.2 Shear Localization is Amplified by a Nonlinear Rheology

The formation of an internal shear band depends sensitively on ice rheology, because different rheology formulations can imply orders of magnitude differences in the response of ice deformation to stresses. Most glacier models adopt Glen's Law with a

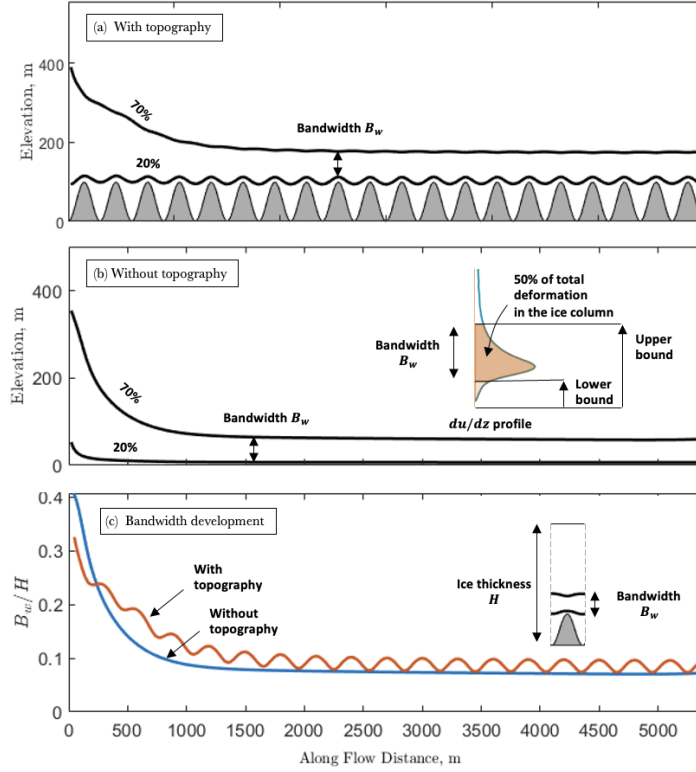


Figure 8. Shear band development along the flow. (a) and (b): The shear band development with and without a topography, defined as a basal zone where the 50% of total deformation in the ice column occurs. Here we use the lower and upper boundary of the shear band to be 20% and 70% of the deformation in the ice column, as illustrated in the subfigure in (b). (c): The ratio of the shear band bandwidth B_w to the ice thickness H at that location along the flow for both cases.

constant exponent connecting strain rate and stress. This uniform treatment may underestimate ice deformation in high-stress regions and overestimation in low-stress regions (Goldsby & Kohlstedt, 2001). To understand how rheology affects shear localization, we compare three different rheology used in ice modeling: a linear Newtonian rheology, Glen’s Law, and the composite rheology by Goldsby and Kohlstedt (2001) as specified in Section 2.2.

The mechanism driving shear-band formation is similar to the creep instability invoked to explain the onset of sliding (Robin, 1955; Clarke et al., 1977; Yuen & Schubert, 1979) with the difference that meltwater would drain out of the shear band over time, suppressing a runaway instability. The thermomechanical coupling driving localization depends on the degree to which ice in the vicinity of topographical highs warms up during flow, as captured in the energy equation (8). Three terms contribute to the thermal evolution: advection, diffusion, and shear heating. To identify the relative magnitude of these terms, we carry out a scaling analysis.

We choose the characteristic parameters to be

$$\bar{z} = H, \quad \bar{\tau} = \rho_i g L_z \alpha, \quad \bar{u} = U_s, \quad \bar{T} = T_0, \quad \bar{\epsilon} = \frac{U_s}{H}, \quad (38)$$

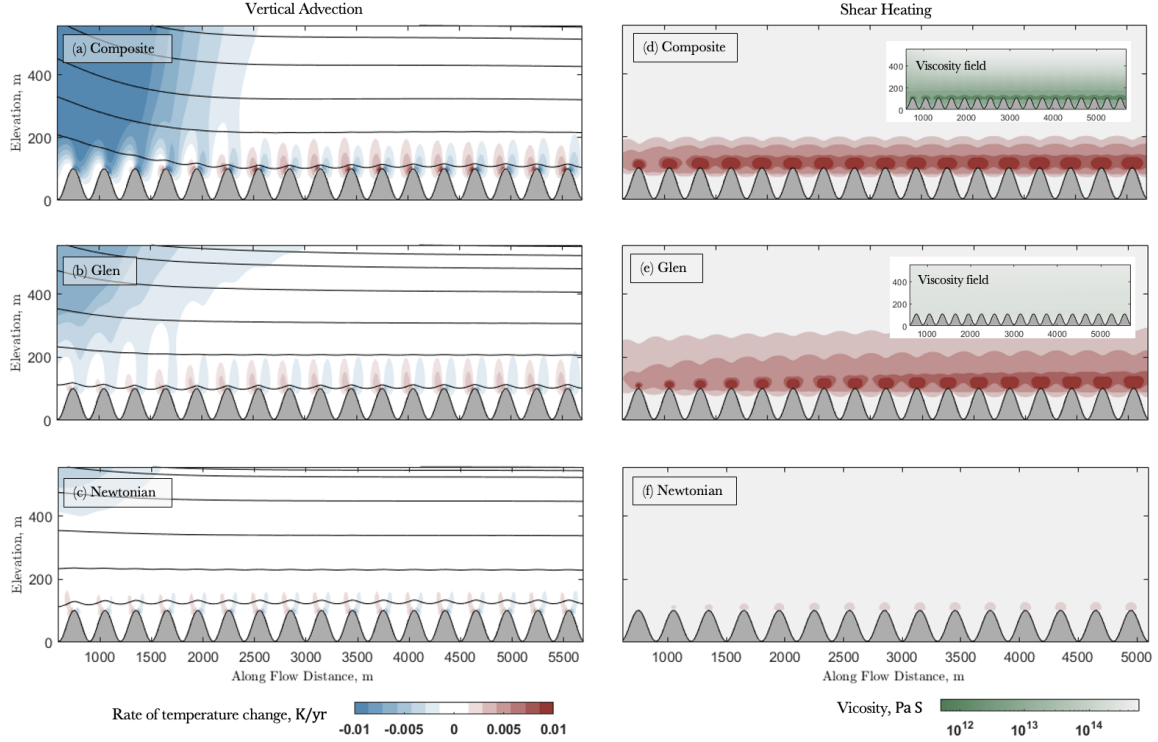


Figure 9. Role of rheology on vertical advection, shear heating, and viscosity localization. Left panel (a), (b) and (c): vertical advection $u_z \partial T / \partial z$ for three cases using Goldsby’s, Glen, and Newtonian rheology, respectively. Blue solid lines denote streamlines. Right panel (d), (e), and (f): modified shear heating $2\tau_E \dot{\epsilon}_E$ presented in the same color scale as the vertical advection. The subfigures (d,1) and (e,1) show the viscosity for the corresponding case in a log scale.

where $H = 1000$ m is the characteristic ice thickness, $U_s = 100$ m/yr is the characteristic surface speed, $T_0 = -26^\circ\text{C}$ is a typical atmospheric temperature in Antarctica, $\alpha = 2^\circ$ is the characteristic bed slope. Other relevant constants are: specific heat of ice $c_p = 2096.9$ J/(kg · K), ice density $\rho_i = 900$ kg/m³, thermal conductivity $\kappa = 2.51$ W/(m · K). As a characteristic vertical speed (or thinning speed), we assume the $U_t \sim U_s \times 10^{-2}$. Substitute in the characteristic values and the constants, we have the scalings of the spatial terms

$$\rho c_p \left(u_i \frac{\partial T}{\partial x_i} \right) \sim \mathcal{O}(10^{-3}), \quad \frac{\partial}{\partial x_i} \left(\kappa \frac{\partial T}{\partial x_i} \right) \sim \mathcal{O}(10^{-5}), \quad \tau_E \dot{\epsilon}_E \sim \mathcal{O}(10^{-3}). \quad (39)$$

Note that in our problem setting of a slab of ice flowing down a slope, the dominant shear strain rate is the shear strain rate $\dot{\epsilon}_{xz}$ and the dominant advection is the vertical advection $U_t(\partial T / \partial z)$.

Figure 9 compares the rate of temperature change from only vertical advection (left panels) to that of only shear heating (right panels) for the three rheology. We adopt the same color scale for the temperature change over time in all panels to enable an easier comparison. In Figure 9 (a-c), we plot only the rate of temperature change associated with the vertical-advection term, $u_z \partial T / \partial z$. The primary effect of vertical advection is cooling, particularly in the left third of the domain, where the streamlines are dipping towards the bed. These streamlines indicate cold ice moving downwards from the ice sur-

face. In the immediate vicinity of topographical highs, however, vertical advection is positive in the upstream side of the obstacle and negative on the downstream side.

In Figure 9 (d-f), we plot the corresponding rate of temperature change associated with the modified shear heating, $2\dot{\epsilon}_E\tau_E/\rho c_p$ on the same color scale as on the left. We refer to this term as “modified” shear heating, because we divide the shear heating term by ice density and specific heat capacity to ensure that it has the same unit as the vertical-advection term, enabling a direct comparison. Modified shear heating is positive throughout the domain and concentrated within the internal shear band extending on top of topographical highs. The rate of heating tends to increase in the downstream direction because the shear heating term $H_s = 2\dot{\epsilon}_E\tau_E$ depends linearly on the local shear strain rate and ice speeds up from upstream to downstream.

A comparison of the panels evidences the profound effect that rheology has both on the spatial distribution of cooling from vertical advection (Figures 9 a-c) and on the magnitude of shear heating (Figures 9 d-f). The composite rheology by Goldsby and Kohlstedt (2001) amplifies both ice thinning and shear heating. In comparison, a Newtonian rheology largely suppresses both effects. For Glen’s Law the spatial distribution of the drawdown and shear heating is similar as for the composite rheology, but both are less pronounced in magnitude (Figures 9 b and e). The primary reason for this difference is that the composite rheology implies a stronger nonlinearity between stress and shear strain rate ($n = 4$ as opposed to $n = 3$ for Glen’s Law) as shown in the viscosity distribution throughout the domain as in the smaller inlets in Figure 9 (d) and (e).

3.3 Shear Heating Dominates the Energy Budget Near topographical highs

The previous section shows that vertical advection and shear heating are the two leading terms governing the energy balance in ice flowing over a topographically variable hard-rock bed. Whether these two processes lead to net cooling or heating depends on both the depth within the ice and the downstream location. Figure 10 shows how the energy balance varies along a streamline starting at $z = 200$ m at the upstream for the three different rheology. Figure 10 (a-c) show how this stream line dips towards the bed to various degrees for different rheology with the most pronounced dip being associated with the composite rheology in panel (a). Figures 10 (d-f) show the evolving energy balance along the streamlines shown on the right (a-c). The blue and red lines in panels (d-f) represent the rate of temperature change associated with vertical advection, the area shaded in dark red captures the shear-heating contribution to temperature and the black line shows the net temperature variation.

For the composite rheology by Goldsby and Kohlstedt (2001), the streamline in (a) descends relatively rapidly to $z = 100$ m over approximately 2 kilometers in the along-flow direction. Thinning then levels off and the elevation of the streamline stabilizes around $z = 100$ m. The rate of temperature change also stabilizes but continues to oscillate at the wavelength imposed by the topography of the bed. In the case of Glen’s law, the initial downward motion of the streamline is much smaller and the ice parcel stabilizes around $z = 180$ (Figure 10 b). The cooling rate associated with vertical advection is about 10 times smaller than for the composite rheology (Figure 10 d). In the Newtonian case, we barely see any downward motion at all (Figure 10 c), suggesting that the streamline of the ice parcel is only minimally affected by topography. Neither vertical advection nor shear heating alter temperature much. The total energy balance consists of small oscillations around zero.

The main insight from Figure 9 is that the magnitude of shear heating differs significantly for the three rheology. Vertical advection differs also, but to a much smaller degree as compared to the two-orders-of-magnitude decrease in shear heating between the Newtonian rheology in panel (f) and the composite rheology in (d). This finding is

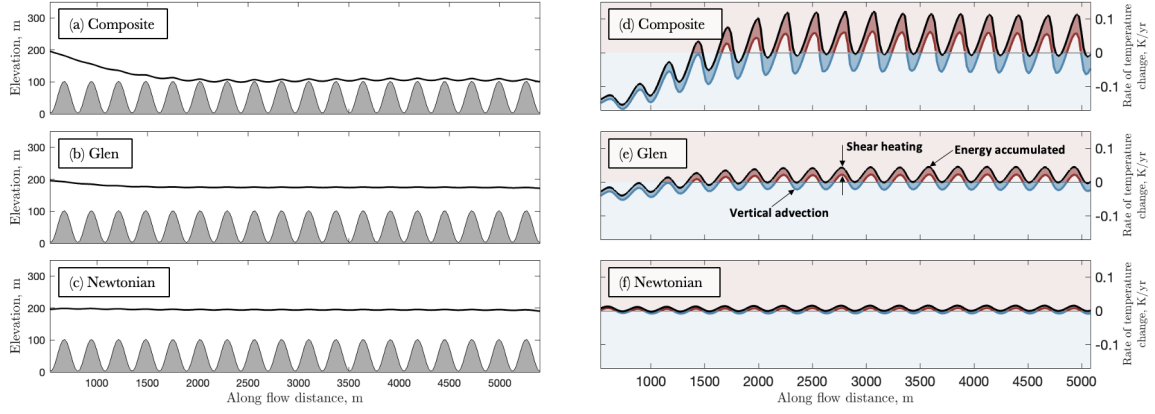


Figure 10. Energy budget along a single streamline. (a-c) Depth of the streamline for the three different rheology. (d-f) Breakdown of the thermal budget along the streamline for the three rheology. The red and blue lines represent the vertical advection (blue line segments indicate cooling, red line segments heating). The areas shaded in dark red represent the contribution of shear heating. The black line shows the net rate of temperature change.

consistent with Figure 9 right panel. The strong dependence of the shear-heating term on rheology, explains why shear heating outweighs the cooling by vertical advection for the composite rheology by Goldsby and Kohlstedt (2001). Evidently, shear heating is particularly pronounced for the streamline selected (Figure 10) because it remains close to the basal topography for most of the domain. For streamlines further away from topographical highs, the effect of shear heating decreases rapidly. An example is the streamline shown for the linear Newtonian case, where shear heating and cooling by vertical advection matter equally (see Figure 10 f).

3.4 Evidence of an Internal Shear Band in Borehole Data from Greenland

In the previous subsections, we show that the inclusion of basal topography may lead to the spontaneous development of an internal shear band through a thermo-mechanical feedbacks. This finding raises the question what the observational signature of an internal shear band would be and how shear band formation could be detected in field data. Here, we compare our model results against observational borehole data by Maier et al. (2019) obtained near the western margin of the Greenland Ice Sheet.

Maier et al. (2019) drilled a network of eight boreholes into a slowly moving ridge located 33 km from the terminus of Issunguata Sermia within the ablation zone of the western margin of the Greenland Ice Sheet. They observe the highest shear strain rates tens of meters above the bed and a rapid decrease of shear strain rate at the bed. We reproduce the depth profile of the measured mean strain rate averaged over all boreholes (Figure 11 a). The data indicates a pronounced increase in shear strain rate at an elevation of tens of meters above the bed followed by a rapid decrease in shear strain rate in the immediate vicinity of the bed.

In top-row panels in Figure 11, we show several model computations of the vertical shear strain rate profile. In Figure 11 (b), we use the same model setup as described so far but change the ice thickness to 650 m, the amplitude of the sinusoidal bed height to 5.5 m and surface temperature to -10°C to match the height where rapid decrease of shear strain rate occurs in the borehole data and a typical Greenland atmospheric tem-

perature. Figure 11 (c) shows the vertical strain rate profile for a control run without basal topography. Figure 11 (d-f) show the velocity profile with depth as inferred by Maier et al. (2019) from measurements (d), obtained from our simulations with basal topography (e), and without (f). All three cases are consistent with the observed surface velocity for the field site, but entail different degrees of internal deformation.

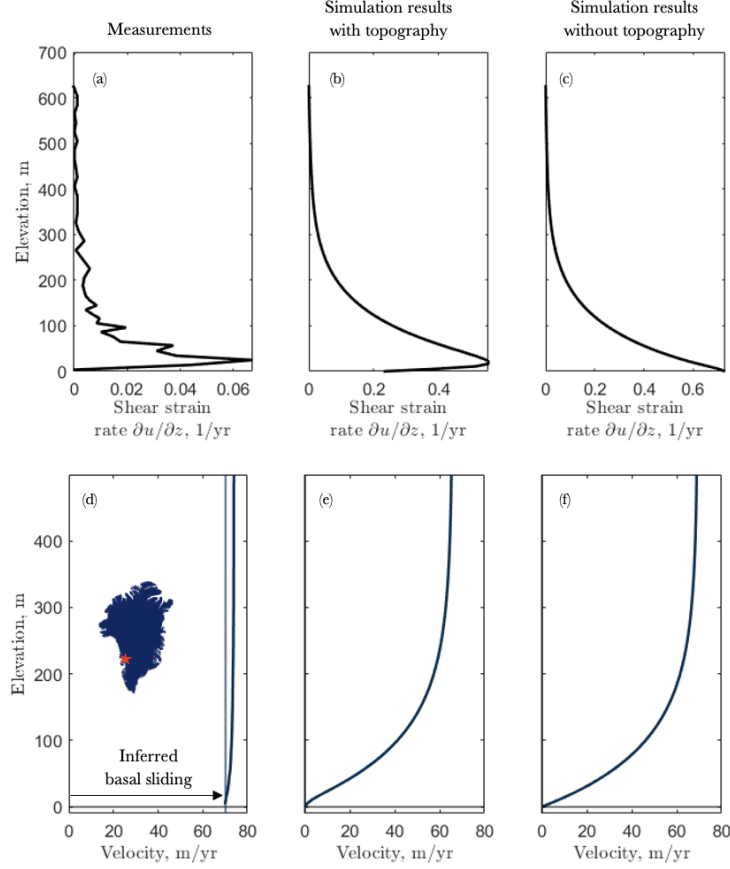


Figure 11. Comparison of our model results to field measurements. The first column is the measurements at West Margin Greenland (Maier et al., 2019), second column is the simulation results with topography, and third row is that without topography. Both simulations use the composite rheology (Goldsby & Kohlstedt, 2001). The first row shows the shear strain rates $\partial u/\partial z$ distribution in the depth direction. The second row show the corresponding velocity profile in the depth direction for each case. In (d), the velocity profile is inferred by integrating the shear strain rate $\partial u/\partial z$ in (a) assuming there is basal sliding (Maier et al., 2019). In the second and third columns, the shear strain rates and velocity profiles are obtained at $x = 4000$ m.

The simulation that includes basal topography in Figure 11 (b) and (e) reproduces a similar shear strain rate profile as seen in the measurements with shear strain rate peaking approximately $z = 25$ m above the bed. In contrast, shear strain rate increases monotonically in the absence of topography as seen in (c). However, the computed shear strain rate is almost an order of magnitude higher than the data. When integrating the measured $\partial u/\partial z$ from the bed to the surface assuming a no-slip boundary at the bed, the internal deformation within the ice suggested by observations is small. One way of reconciling this disconnect would be to invoke basal sliding as suggested by Maier et al. (2019).

Maier et al. (2019) argue that the difference between the surface velocity of around 70 m/yr and the integrated deformational velocity represents basal sliding, as shown in (d).

We propose that the borehole data obtained by Maier et al. (2019) affords two interesting insights into the ice dynamics at the field site. We agree with their interpretation that basal sliding dominates the relatively slow flowing part of Issunguata Sermia. However, basal sliding does not explain the observed peak in shear strain rate followed by a decrease to approximately zero shear strain rate at bed. We propose that the shear strain rate peak could constitute the remnant of an internal shear band that might have formed upstream when ice was flowing of a topographically variable bed, potentially facilitating the transition from flow-to-sliding.

4 Discussion

The fast speeds of many glaciers and ice streams are thought to be accommodated by basal sliding with internal deformation contributing only minimally (Echelmeyer & Zhongxiang, 1987; Hermann & Barclay, 1998; Rignot et al., 2011; Rignot & Mouginot, 2012). However, recent advances in our understanding of the different deformational regime of ice particularly at high stresses (Goldsby & Kohlstedt, 2001) and a growing appreciation for the sharp weakening of ice near pre-melting conditions (Krabbendam, 2016) merit a re-evaluation of the degree to which internal deformation may contribute to fast ice motion. Similarly, it is important to identify the physical processes that control the spatial scale over which the flow-to-sliding transition occurs to improve ice-sheet models (Bueler & Brown, 2009).

Acceleration of ice flow does not necessarily lead to basal sliding, because it causes the ice to thin, bringing cold ice closer to the bed and refreezing the bed. This refreeze or freeze-on phenomenon has been theoretically studied, simulated, and observed (e.g., Kamb, 2001; Vogel et al., 2003; Mantelli et al., 2019; Mantelli & Schoof, 2019). The refreeze hinges sensitively on ice rheology and the spatial scale over which the transition to sliding occurs. In our simulations, we do not observe refreezing of the bed, because internal shear heating compensates for the cooling effect of vertical advection, particularly for the composite rheology by Goldsby and Kohlstedt (2001). The important role of rheology is not surprising given that a higher power-law exponent between stress and shear strain rate, enhances the positive feedback between deformation, viscosity weakening and shear heating (Clarke et al., 1977).

We identify two competing mechanisms that control the development of an internal shear band: vertical advection and shear heating. We conclude that an internal shear band forms when shear heating eclipses the cooling effect of vertical advection, resulting in a positive energy balance above the topographical highs as ice flows downstream. We show that vertical advection is proportional to the rate of thinning and therefore the rate of glacier acceleration. When this shear heating dominates over the vertical advection, the net energy gain in the shear band region becomes positive and an internal shear band forms. On the contrary, when shear heating does not compensate for the cold down-draw, the net energy gain is negative or oscillates around a very small value, and the shear band formation is suppressed.

The presence of basal topography amplifies shear heating, because it causes additional deformation within the ice. Importantly, this deformation is not reduced but instead amplified by acceleration as ice is forced to wrap around topographical highs at increasing speed. In comparison, basal sliding is initiated when basal strain rates are large, favoring heat production and lubricating the bed (e.g., Lüthi et al., 2002; Shapero et al., 2016). The dilemma is that after initiation, deformation within the basal ice decreases and shear heating is reduced. Frictional heating may partially compensate for the loss

of shear heating, but observations suggest that high surface speeds can be achieved with relatively small basal stresses (MacAyeal et al., 1995; Joughin et al., 2004, 2006).

We emphasize that the high-degree of shear localization occurring within an internal shear band does not represent sliding. Ice would still be frozen to the bed when the internal shear band forms, but the internal shear band gradually warms basal ice; potentially to the degree that the ice-bedrock interface transitions to sliding. This finding suggests that sub-temperature sliding might not be the only way to transit from slow-to-fast ice flow (Mantelli & Schoof, 2019).

The possibility of high basal shear stress around topographical highs inferred here may also have implication for variations in ice fabric. For example, borehole data of grain size and cone angles collected at Siple Dome Antarctica by DiPrinzio et al. (2005) and reanalyzed by Pettit et al. (2011) reveals a localized band of small ice crystals and highly oriented fabric, located several hundred meters above the bed. Several processes could contribute to the development of this ice fabric with stress being a prominent factor, as supported by strain rate data. However, the observed shift in fabric occurs around the depth of the Holocene transition, highlighting that climate history may also play a role (Pettit et al., 2011). Despite its age, this ice fabric continues to control ice flow by partially decoupling of the flow field above and below the shear band. The flow field becomes three-dimensional, potentially to the degree of eddies forming (Meyer & Creyts, 2017).

Apart from altering the stress distribution within the ice column, our model also suggests a multi-dimensional stress field in the immediate vicinity of the bed rock, which could be relevant for our understanding of erosional processes and the transport of subglacial debris. Glaciers erode the underlying bedrock by abrasion (Bernard, 1979; Hallet, 1996). The ice-induced stresses on bedrock surfaces constitutes the dominant contribution to this eroding force (Bernard, 1979). Our results show that shear stress is concentrated around topographical highs. Variable thermal conditions at this location could further amplify the preferential erosion of topographical highs. We emphasize that in our model the bedrock itself does not evolve, so we do not capture the long-term feedback between ice motion and hard-rock erosion here.

Another limitation is that we only consider a highly simplified, sinusoidal bedrock shape. In reality, basal topography is a lot more variable as summarized in Figure 12 for NEGIS, Institute, and Byrd. The figure summarizes basal topography, basal roughness and associated surface speed near the onset of these three zones of fast ice motion. To better visualize the roughness and its correlation to surface speed, we adopt the approach by Li et al. (2010) and Cooper et al. (2019) to characterize the basal roughness using two parameters: dominant wavelength and vertical roughness within a defined window along the stream. The dominant vertical roughness is defined as the root mean square of the deviation of the bedrock shape from its mean elevation and the dominant wavelength is

$$\zeta = \frac{1}{n-1} \left[\sum_{i=1}^n (z(x_i) - \bar{z})^2 \right], \quad \xi = \frac{1}{k(\hat{z})|_{\hat{z}_{\max}}}, \quad (40)$$

where n is the number of sample points, $z(x_i)$ is the bedrock elevation, \bar{z} is the mean value of the bedrock elevation, and $k(\hat{z})$ is the Fourier transform of z .

To compute the dominant wavelength, we simply extract the wavelength of the topography which has the maximum value in the frequency space within that window. Intuitively, the larger the vertical roughness, the rougher the bedrock, and the shorter the dominant wavelength, the rougher the bedrock. Figure 12 (d-f) show the correlation of the dominant wavelength and the surface speed. We can see that for all three ice streams, the dominant wavelength is negatively related to surface speed, shown as the black solid

lines. Although this is a very qualitative analysis, it reveals a commonality between these three locations, namely that fast the ice motion correlates with short dominant wavelengths of the basal topography. This is consistent with our model results, where basal topography facilitates the fast ice motion through the spontaneously developed internal shear band.

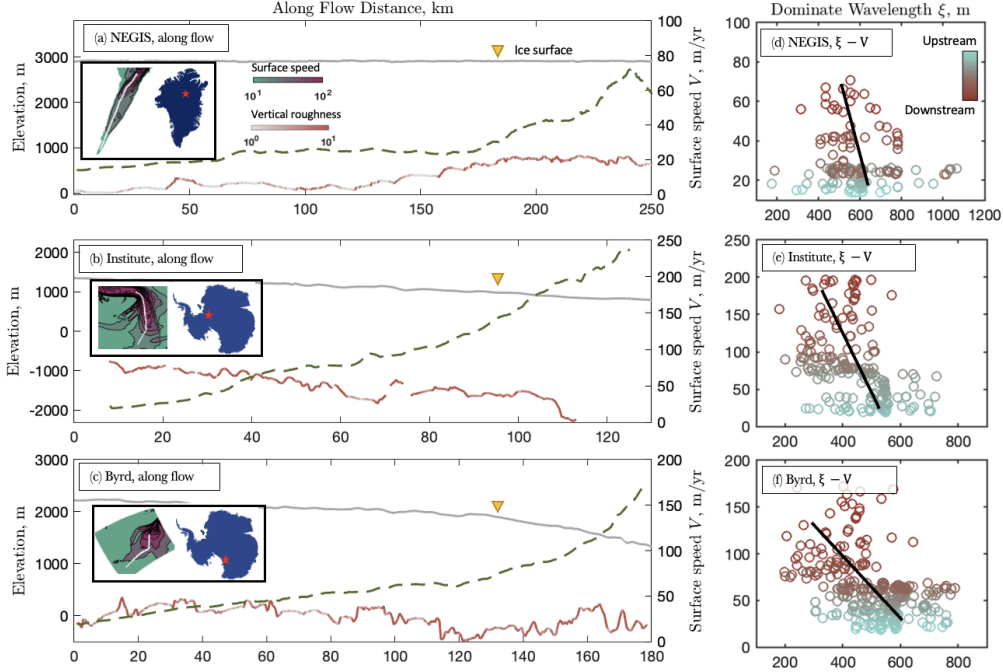


Figure 12. Surface velocities change with the basal topography along streamline, and the dominant wavelength at Institute Ice Stream(a), Byrd Ice Stream(b), and NEGIS(c). Ice surface speed, basal topography, ice surface are plotted in dashed lines, grey lines, and red-white solid lines, respectively. The ice surface speed at the corresponding dominant wavelength along the flow is shown on the right panel.

The correlation of the basal topography and fast ice motion shows that the ability of ice models to include basal topography and resolve the interaction between ice and bedrock is critical. This helps reveal the significance of irregular basal shape in the physical process of shear heating generation inside the ice, which further leads to the development of internal shear band. The important role that topography is highlighted by the result that an internal shear band does not always form. If a linear rheology is used, or two consecutive bumps are too distant to each other, cooling in between bumps dominates over shear at each bump, destroying the connection.

5 Conclusion

In this paper, we build upon the thermo-mechanical Stokes flow model developed by Räss et al. (2020) by incorporating a basal topography and a free surface. We use the Immersed Boundary Methods and the Level Set Methods to resolve the ice-bedrock interface and ice-air interface. We simulate ice flows over a sinusoidal basal topography that undergoes thinning, and compare the results with a control case that has a flat topography. We find that the inclusion of basal topography may lead to extensive shear

localization on topographical highs. As a result, an internal shear band forms as supported by borehole data in Greenland (Maier et al., 2019). We investigate three different constitutive relations: a Newtonian, a power law (Glen, 1952), and a composite rheology by Goldsby and Kohlstedt (2001). We find that a non-linear rheology amplifies shear heating more strongly than advective cooling, tilting the energy balance towards heating in the basal region of ice. We conclude that basal topography could trigger internal shear localizations and may potentially enable a transition from flow-to-sliding over a spatially extended zone. Our work could inform existing ice-sheet models like Bueler and Brown (2009) by relating the spatial scale over which the transition to sliding occurs to the topography of the bedrock underneath the ice.

6 Open Research

The current version of the numerical thermo-mechanical model with a build-in non-linear rheology model is available from DOI repository (Zenodo) at: <https://doi.org/10.5281/zenodo.7392224>. This model is developed based on the FastIce that can be found at: <https://doi.org/10.5281/zenodo.3461171> (Räss et al., 2020). The borehole data of shear deformation in Figure 11 (a) to compare against simulation results can be found from Maier et al. (2019). The basal topography data in Figure 1 (a) and Figure 12 (b-c) can be found at: <https://nsidc.org/data/adbmg4/versions/5> (Morlighem et al., 2017). The ice surface speed data in Figure 1 (b) and Figure 12 can be found at: [10.5067/MEASURES/CRYOSPHERE/nsidc-0478.001](https://doi.org/10.5067/MEASURES/CRYOSPHERE/nsidc-0478.001) (Joughin, Smith, Howat, & Scambos, 2010). The basal topography data in Figure 1 (c) and Figure 12 (a) can be found at: <https://doi.pangaea.de/10.1594/PANGAEA.907918> (Franke et al., 2021).

Acknowledgments

This work was supported by the NSF CAREER grant # 2142651. We acknowledge helpful conversations about this work with Paul Summers, Daniel Martin, Dustin Schroeder, Eric Dunham, and Elisa Mantelli.

References

- Adalsteinsson, D., & Sethian, J. A. (1999). The fast construction of extension velocities in level set methods. *Journal of Computational Physics*, 148(1), 2–22.
- Bamber, J. L., Layberry, R. L., & Gogineni, S. (2001). A new ice thickness and bed data set for the greenland ice sheet: 1. measurement, data reduction, and errors. *Journal of Geophysical Research: Atmospheres*, 106(D24), 33773–33780.
- Bernard, H. (1979). A theoretical model of glacial abrasion. *Journal of Glaciology*, 23(89), 39–50.
- Bindschadler, R. (2006). The environment and evolution of the west antarctic ice sheet: setting the stage. *Philosophical Transactions of the Royal Society A: Mathematical, Physical and Engineering Sciences*, 364(1844), 1583–1605.
- Bingham, R. G., & Siegert, M. J. (2007). Radar-derived bed roughness characterization of institute and möller ice streams, west antarctica, and comparison with siple coast ice streams. *Geophysical Research Letters*, 34(21).
- Bueler, E., & Brown, J. (2009). Shallow shelf approximation as a “sliding law” in a thermomechanically coupled ice sheet model. *Journal of Geophysical Research: Earth Surface*, 114(F3).
- Clarke, G. K. (1987). Fast glacier flow: Ice streams, surging, and tidewater glaciers. *Journal of Geophysical Research: Solid Earth*, 92(B9), 8835–8841.
- Clarke, G. K., Nitsan, U., & Paterson, W. (1977). Strain heating and creep instability in glaciers and ice sheets. *Reviews of geophysics*, 15(2), 235–247.
- Cooper, M. A., Jordan, T. M., Schroeder, D. M., Siegert, M. J., Williams, C. N., & Bamber, J. L. (2019). Subglacial roughness of the greenland ice sheet: relationship with contemporary ice velocity and geology. *The Cryosphere*, 13(11), 3093–3115.
- DiPrinzio, C., Wilen, L. A., Alley, R., Fitzpatrick, J., Spencer, M., & Gow, A. (2005). Fabric and texture at siple dome, antarctica. *Journal of Glaciology*, 51(173), 281–290.
- Doyle, S. H., Hubbard, B., Christoffersen, P., Young, T. J., Hofstede, C., Bougamt, M., ... Hubbard, A. (2018). Physical conditions of fast glacier flow: 1. measurements from boreholes drilled to the bed of store glacier, west greenland. *Journal of Geophysical Research: Earth Surface*, 123(2), 324–348.
- Duval, P., et al. (1977). The role of the water content on the creep rate of polycrystalline ice. *IAHS Publ*, 118, 29–33.
- Echelmeyer, K., & Zhongxiang, W. (1987). Direct observation of basal sliding and deformation of basal drift at sub-freezing temperatures. *Journal of Glaciology*, 33(113), 83–98.
- Fowler. (2001). Modelling the flow of glaciers and ice sheets. In *Continuum mechanics and applications in geophysics and the environment* (pp. 201–221). Springer.
- Fowler. (2010). Weertman, liboutry and the development of sliding theory. *Journal of Glaciology*, 56(200), 965–972.
- Fowler, & Larson. (1980). The uniqueness of steady state flows of glaciers and ice sheets. *Geophysical Journal International*, 63(2), 333–345.
- Franke, S., Jansen, D., Beyer, S., Neckel, N., Binder, T., Paden, J., & Eisen, O. (2021). Complex basal conditions and their influence on ice flow at the onset of the northeast greenland ice stream. *Journal of Geophysical Research: Earth Surface*, 126(3), e2020JF005689.
- Gagliardini, O., Zwinger, T., Gillet-Chaulet, F., Durand, G., Favier, L., De Fleurian, B., ... others (2013). Capabilities and performance of elmer/ice, a new-generation ice sheet model. *Geoscientific Model Development*, 6(4), 1299–1318.
- Glen. (1952). Experiments on the deformation of ice. *Journal of Glaciology*, 2(12), 111–114.

- Glen. (1955). The creep of polycrystalline ice. *Proceedings of the Royal Society of London. Series A. Mathematical and Physical Sciences*, 228(1175), 519–538.
- Goldsby, D., & Kohlstedt, D. L. (2001). Superplastic deformation of ice: Experimental observations. *Journal of Geophysical Research: Solid Earth*, 106(B6), 11017–11030.
- Greve, R. (1997a). Application of a polythermal three-dimensional ice sheet model to the greenland ice sheet: response to steady-state and transient climate scenarios. *Journal of Climate*, 10(5), 901–918.
- Greve, R. (1997b). A continuum–mechanical formulation for shallow polythermal ice sheets. *Philosophical Transactions of the Royal Society of London. Series A: Mathematical, Physical and Engineering Sciences*, 355(1726), 921–974.
- Hallet, B. (1996). Glacial quarrying: A simple theoretical model. *Annals of Glaciology*, 22, 1–8.
- Hermann, E., & Barclay, K. (1998). Basal sliding of ice stream b, west antarctica. *Journal of Glaciology*, 44(147), 223–230.
- Joughin, I., Bamber, J. L., Scambos, T., Tulaczyk, S., Fahnestock, M., & MacAyeal, D. R. (2006). Integrating satellite observations with modelling: basal shear stress of the filcher-ronne ice streams, antarctica. *Philosophical Transactions of the Royal Society A: Mathematical, Physical and Engineering Sciences*, 364(1844), 1795–1814.
- Joughin, I., MacAyeal, D. R., & Tulaczyk, S. (2004). Basal shear stress of the ross ice streams from control method inversions. *Journal of Geophysical Research: Solid Earth*, 109(B9).
- Joughin, I., Rignot, E., Rosanova, C. E., Lucchitta, B. K., & Bohlander, J. (2003). Timing of recent accelerations of pine island glacier, antarctica. *Geophysical Research Letters*, 30(13).
- Joughin, I., Smith, B., Howat, I., & Scambos, T. (2010). Measures greenland ice sheet velocity map from insar data, version 2. *NASA National Snow and Ice Data Center Distributed Active Archive Center, Boulder, Colorado, USA (doi: 10.5067/MEASURES/CRYOSPHERE/nsidc-0478.001)*.
- Joughin, I., Smith, B. E., Howat, I. M., Scambos, T., & Moon, T. (2010). Greenland flow variability from ice-sheet-wide velocity mapping. *Journal of Glaciology*, 56(197), 415–430.
- Kamb, B. (2001). Basal zone of the west antarctic ice streams and its role in lubrication of their rapid motion. *The West Antarctic ice sheet: behavior and environment*, 77, 157–199.
- Krabbendam, M. (2016). Sliding of temperate basal ice on a rough, hard bed: creep mechanisms, pressure melting, and implications for ice streaming. *The Cryosphere*, 10(5), 1915–1932.
- Kreiss, H.-O. (1968). Stability theory for difference approximations of mixed initial boundary value problems. i. *Mathematics of Computation*, 22(104), 703–714.
- Li, X., Sun, B., Siegert, M. J., Bingham, R. G., Tang, X., Zhang, D., . . . Zhang, X. (2010). Characterization of subglacial landscapes by a two-parameter roughness index. *Journal of Glaciology*, 56(199), 831–836.
- Lliboutry, L. (1968). General theory of subglacial cavitation and sliding of temperate glaciers. *Journal of Glaciology*, 7(49), 21–58.
- Lüthi, M., Funk, M., Iken, A., Gogineni, S., & Truffer, M. (2002). Mechanisms of fast flow in jakobshavn isbræ, west greenland: Part iii. measurements of ice deformation, temperature and cross-borehole conductivity in boreholes to the bedrock. *Journal of Glaciology*, 48(162), 369–385.
- MacAyeal, D. R., Bindshadler, R. A., & Scambos, T. A. (1995). Basal friction of ice stream e, west antarctica. *Journal of Glaciology*, 41(138), 247–262.
- Maier, N., Humphrey, N., Harper, J., & Meierbachtol, T. (2019). Sliding dominates slow-flowing margin regions, greenland ice sheet. *Science advances*, 5(7), eaaw5406.

- Mantelli, E., Haseloff, M., & Schoof, C. (2019). Ice sheet flow with thermally activated sliding. part 1: the role of advection. *Proceedings of the Royal Society A*, 475(2230), 20190410.
- Mantelli, E., & Schoof, C. (2019). Ice sheet flow with thermally activated sliding. part 2: the stability of subtemperate regions. *Proceedings of the Royal Society A*, 475(2231), 20190411.
- Martin, M., Winkelmann, R., Haseloff, M., Albrecht, T., Bueler, E., Khroulev, C., & Levermann, A. (2011). The potsdam parallel ice sheet model (pism-pik)–part 2: dynamic equilibrium simulation of the antarctic ice sheet. *The Cryosphere*, 5(3), 727–740.
- McCarthy, C., Savage, H., & Nettles, M. (2017). Temperature dependence of ice-on-rock friction at realistic glacier conditions. *Philosophical Transactions of the Royal Society A: Mathematical, Physical and Engineering Sciences*, 375(2086), 20150348.
- Meyer, C. R., & Creyts, T. T. (2017). Formation of ice eddies in subglacial mountain valleys. *Journal of Geophysical Research: Earth Surface*, 122(9), 1574–1588.
- Morlighem, M., Williams, C. N., Rignot, E., An, L., Arndt, J. E., Bamber, J. L., ... others (2017). Bedmachine v3: Complete bed topography and ocean bathymetry mapping of greenland from multibeam echo sounding combined with mass conservation. *Geophysical research letters*, 44(21), 11–051.
- Mouginot, J., Rignot, E., & Scheuchl, B. (2014). Sustained increase in ice discharge from the amundsen sea embayment, west antarctica, from 1973 to 2013. *Geophysical Research Letters*, 41(5), 1576–1584.
- Nye. (1959). The motion of ice sheets and glaciers. *Journal of Glaciology*, 3(26), 493–507.
- Nye. (1969). A calculation on the sliding of ice over a wavy surface using a newtonian viscous approximation. *Proceedings of the Royal Society of London. A. Mathematical and Physical Sciences*, 311(1506), 445–467.
- Nye. (1971). Causes and mechanics of glacier surges: discussion. *Canadian Journal of Earth Sciences*, 8(2), 306–307.
- Orlanski, I. (1976). A simple boundary condition for unbounded hyperbolic flows. *Journal of computational physics*, 21(3), 251–269.
- Osher, S., Fedkiw, R., & Piechor, K. (2004). Level set methods and dynamic implicit surfaces. *Appl. Mech. Rev.*, 57(3), B15–B15.
- Osher, S., & Sethian, J. A. (1988). Fronts propagating with curvature-dependent speed: Algorithms based on hamilton-jacobi formulations. *Journal of computational physics*, 79(1), 12–49.
- Paterson, W. S. B. (1994). *Physics of glaciers*. Butterworth-Heinemann.
- Peskin. (1972). *Flow patterns around heart valves: a digital computer method for solving the equations of motion*. Yeshiva University.
- Peskin. (2002). The immersed boundary method. *Acta Numerica*, 11, 479–517. Retrieved from <https://doi.org/10.1080/00207540701450013> doi: doi:10.1017/S0962492902000077
- Petrat, N., Zhu, H., Stadler, G., Hughes, T. J., & Ghattas, O. (2012). An inexact gauss-newton method for inversion of basal sliding and rheology parameters in a nonlinear stokes ice sheet model. *Journal of Glaciology*, 58(211), 889–903.
- Pettit, E. C., Waddington, E. D., Harrison, W. D., Thorsteinsson, T., Elsberg, D., Morack, J., & Zumbege, M. A. (2011). The crossover stress, anisotropy and the ice flow law at siple dome, west antarctica. *Journal of Glaciology*, 57(201), 39–52.
- Qin, Z., Delaney, K., Riaz, A., & Balaras, E. (2015). Topology preserving advection of implicit interfaces on cartesian grids. *Journal of Computational Physics*, 290, 219–238.
- Räss, L., Licul, A., Herman, F., Podladchikov, Y. Y., & Suckale, J. (2020). Mod-

- elling thermomechanical ice deformation using an implicit pseudo-transient method (fastice v1. 0) based on graphical processing units (gpus). *Geoscientific Model Development*, 13(3), 955–976.
- Rignot, E., & Mouginot, J. (2012). Ice flow in greenland for the international polar year 2008–2009. *Geophysical Research Letters*, 39(11).
- Rignot, E., Mouginot, J., & Scheuchl, B. (2011). Ice flow of the antarctic ice sheet. *Science*, 333(6048), 1427–1430.
- Rignot, E., Vaughan, D. G., Schmelz, M., Dupont, T., & MacAyeal, D. (2002). Acceleration of pine island and thwaites glaciers, west antarctica. *Annals of Glaciology*, 34, 189–194.
- Robin. (1955). Ice movement and temperature distribution in glaciers and ice sheets. *Journal of Glaciology*, 2(18), 523–532.
- Räss, L., Utkin, I., Duretz, T., Omlin, S., & Podladchikov, Y. Y. (2022, July). Assessing the robustness and scalability of the accelerated pseudo-transient method. *Geoscientific Model Development*, 15(14), 5757–5786. Retrieved 2022-10-19, from <https://gmd.copernicus.org/articles/15/5757/2022/> doi: 10.5194/gmd-15-5757-2022
- Schmid, D. W., & Podladchikov, Y. Y. (2003). Analytical solutions for deformable elliptical inclusions in general shear. *Geophysical Journal International*, 155(1), 269–288.
- Schoof, C. (2005). The effect of cavitation on glacier sliding. *Proceedings of the Royal Society A: Mathematical, Physical and Engineering Sciences*, 461(2055), 609–627.
- Sethian, J. A. (1999). *Level set methods and fast marching methods: evolving interfaces in computational geometry, fluid mechanics, computer vision, and materials science* (Vol. 3). Cambridge university press.
- Sethian, J. A., & Smereka, P. (2003). Level set methods for fluid interfaces. *Annual review of fluid mechanics*, 35(1), 341–372.
- Shapero, D. R., Joughin, I. R., Poinar, K., Morlighem, M., & Gillet-Chaulet, F. (2016). Basal resistance for three of the largest greenland outlet glaciers. *Journal of Geophysical Research: Earth Surface*, 121(1), 168–180.
- Siegert, M. J., Taylor, J., Payne, A. J., & Hubbard, B. (2004). Macro-scale bed roughness of the siiple coast ice streams in west antarctica. *Earth Surface Processes and Landforms: The Journal of the British Geomorphological Research Group*, 29(13), 1591–1596.
- Suckale, J., Platt, J. D., Perol, T., & Rice, J. R. (2014). Deformation-induced melting in the margins of the west antarctic ice streams. *Journal of Geophysical Research: Earth Surface*, 119(5), 1004–1025.
- Uhlmann, M. (2005). An immersed boundary method with direct forcing for the simulation of particulate flows. *Journal of computational physics*, 209(2), 448–476.
- Vogel, S. W., Tulaczyk, S., & Joughin, I. R. (2003). Distribution of basal melting and freezing beneath tributaries of ice stream c: implication for the holocene decay of the west antarctic ice sheet. *Annals of Glaciology*, 36, 273–282.
- Weertman, J. (1957). On the sliding of glaciers. *Journal of glaciology*, 3(21), 33–38.
- Whillans, I., Bolzan, J., & Shabtaie, S. (1987). Velocity of ice streams b and c, antarctica. *Journal of Geophysical Research: Solid Earth*, 92(B9), 8895–8902.
- Winkelmann, R., Martin, M. A., Haseloff, M., Albrecht, T., Bueler, E., Khroulev, C., & Levermann, A. (2011). The potsdam parallel ice sheet model (pism-pik)–part 1: Model description. *The Cryosphere*, 5(3), 715–726.
- Yuen, D. A., & Schubert, G. (1979). The role of shear heating in the dynamics of large ice masses. *Journal of Glaciology*, 24(90), 195–212.